Supporting Information for

"Ir/IrO_x/WO_3 Electrocatalysts for Water Splitting"

Xiaohe Tan,[a, b] Wangyan Gou,[b] Linqing Liao,[b] Yuanyuan Ma*[a,b] and Yongquan Qu*[b]

[a.] Research & Development Institute of Northwestern Polytechnical University in Shenzhen, Shenzhen, 518057, China.

[b.] School of Chemistry and Chemical Engineering, Northwestern Polytechnical University, Xi'an, 710072, China.

Email: yyma@nwpu.edu.cn and yongquan@nwpu.edu.cn

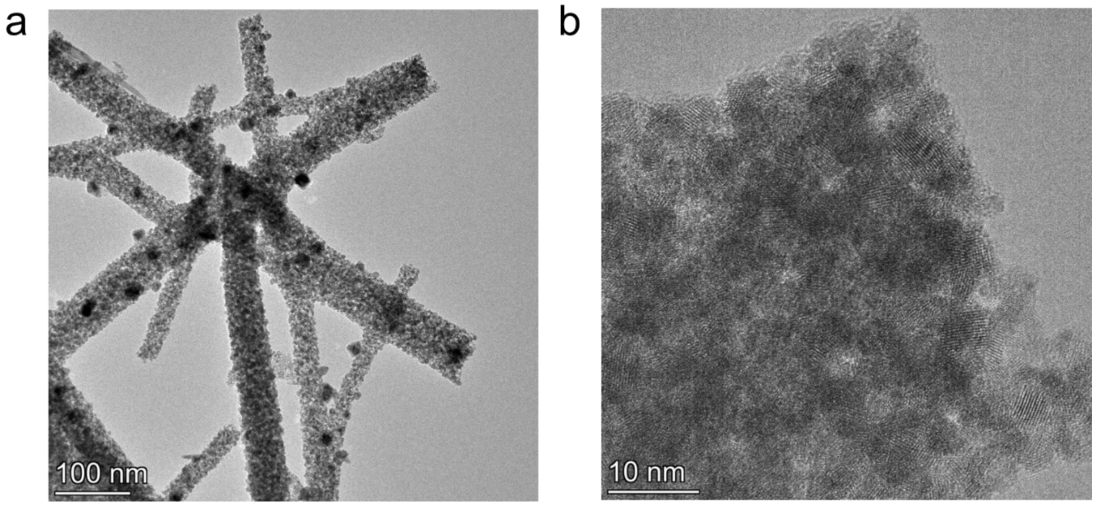

Fig. S1. (a) TEM image and (b) HRTEM image of $Ir/IrO_x/WO_3$-550.

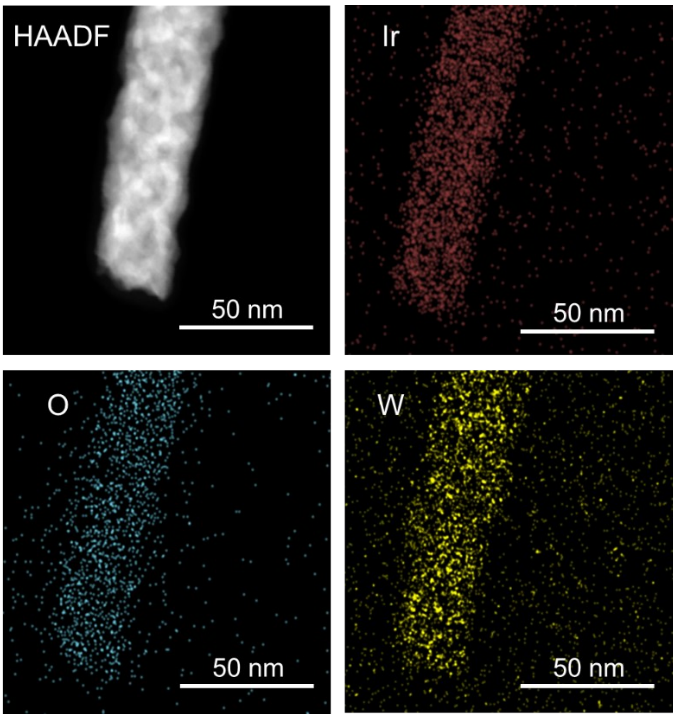

Fig. S2. Elemental X-ray mapping images of $Ir/IrO_x/WO_3$-350.

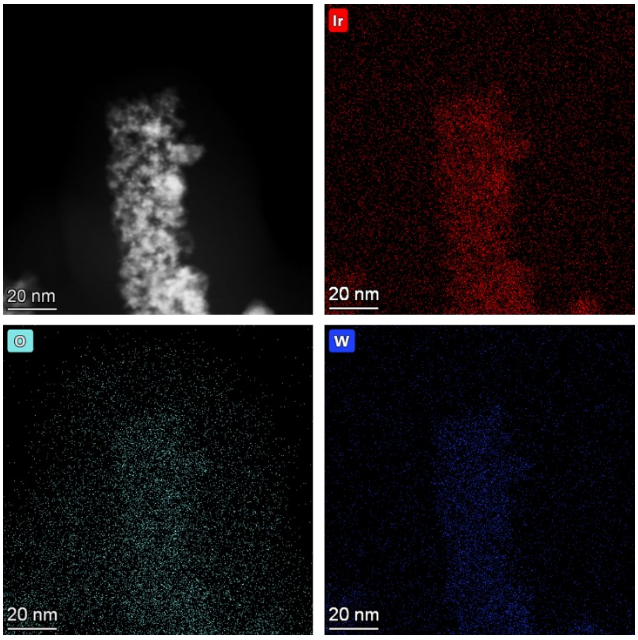

Fig. S3. Elemental X-ray mapping images of IrO_x/WO_3-550.

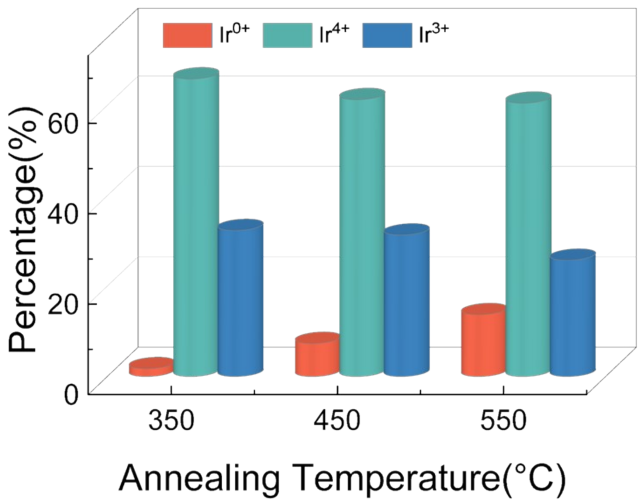

Fig. S4. The proportions of various oxidation states of Ir as-synthesized $Ir/IrO_x/WO_3$ electrocatalysts.

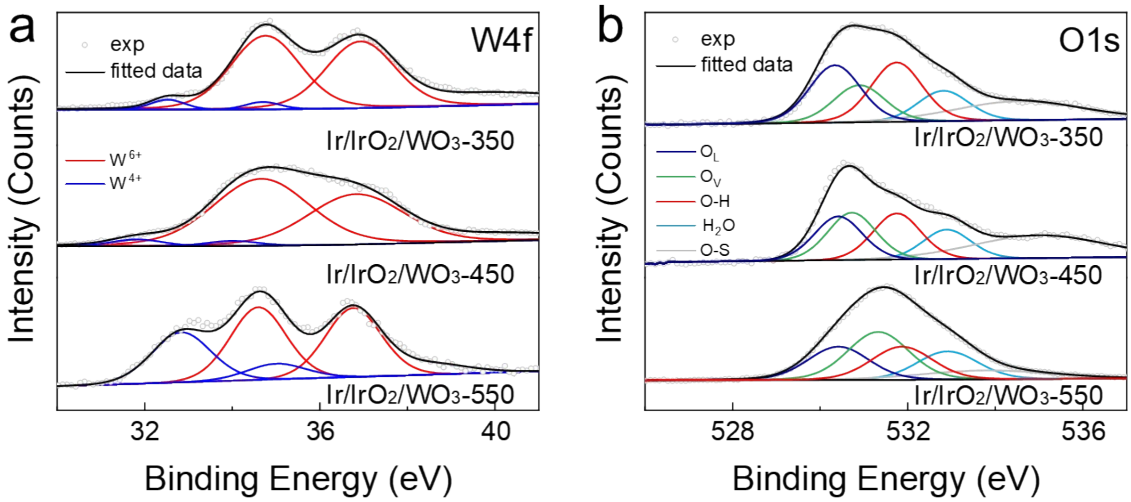

Fig. S5. (a) W 4f XPS spectra and (b) O1s XPS spectra of as-synthesized IrO_x/WO_3.

Table S1. The proportion statistics of iridium species from Ir 4f XPS spectra.

Catalyst	Ir^0	Ir^{3+}	Ir^{4+}
$Ir/IrO_x/WO_3$-350	1.77	32.34	65.89
$Ir/IrO_x/WO_3$-450	7.35	31.34	61.31
$Ir/IrO_x/WO_3$-550	13.72	25.76	60.52

Table S2. The proportion statistics of tungsten species from W 4f XPS spectra.

Catalyst	W^{6+}	W^{4+}
$Ir/IrO_x/WO_3$-350	94.22	5.78
$Ir/IrO_x/WO_3$-450	94.88	5.12
$Ir/IrO_x/WO_3$-550	67.08	32.92

Table S3. The proportion statistics of oxygen species from O 1s XPS spectra.

Catalyst	H_2O	S-O	O_L	O-H	O_V
$Ir/IrO_x/WO_3$-350	13.19	20.13	24.86	25.72	16.10
$Ir/IrO_x/WO_3$-450	12.80	27.49	19.00	20.09	20.62
$Ir/IrO_x/WO_3$-550	17.52	11.66	20.61	20.53	29.69

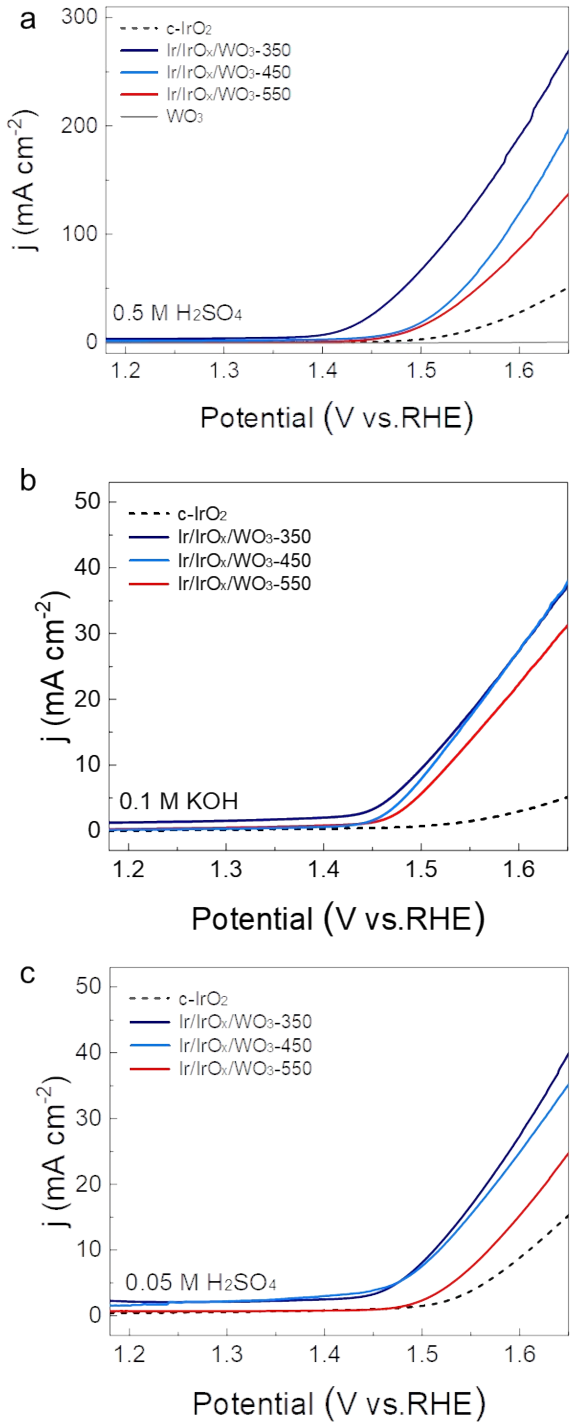

Fig. S6. Polarization curves (current density normalized by the geometric areas of the electroactive materials) of the as-synthesized $Ir/IrO_x/WO_3$ and c-IrO_2 in (a) 0.5 M H_2SO_4; (b) 0.1 M KOH; (c) 0.05M H_2SO_4.

Table S4. Summary of Ir-based catalysts as OER electrocatalysts.

Catalyst	Electrolyte	Overpotential at 10 mA cm^{-2} (mV)	Stability at 10 mA cm^{-2} (h)	Ref
$Ir/IrO_x/WO_3$	0.5M H_2SO_4; 1.0 M KOH	185; 232	80	This work
Ir_1@Co/NC	1.0 M KOH	260	5	1
Ir_{SA}-NiO	1.0 M KOH	215	10	2
Ir_{SA}-CoO_x ANSs	1.0 M KOH	152 ± 5.2	10	3
Ir–CoM LDHs (M = Ni, Fe, Mn, and Zn)	1.0 M KOH	262	60	4
IrRu@Te	0.5M H_2SO_4	220	20	5
IrO_2@Ir/TiN	0.5M H_2SO_4	265	6	6
ATO-supported Ir NDs	0.05M H_2SO_4	280	15	7
Ru@IrO_x	0.05M H_2SO_4	282	24	8
Ir–MnO_2	0.5M H_2SO_4	218	650	9
TiN/IrO_2	0.5M H_2SO_4	313	3	10
Ir–W@Ir–WO_{3-x}	0.5M H_2SO_4	261	20	11
IrO_2/GCN	0.5M H_2SO_4	276	5	12
AA-IrO_x	0.5M H_2SO_4	370	8	13
Au@$AuIr_2$	0.5M H_2SO_4	-	40	14
Ir-SA@Fe@NCNT	0.5M H_2SO_4	250	12	15

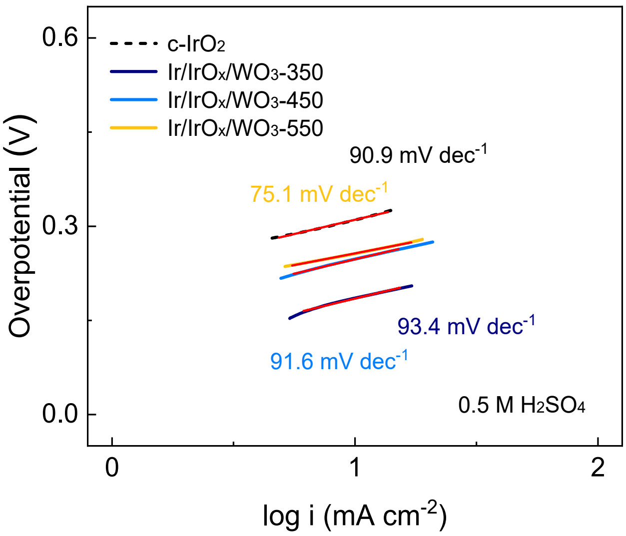

Fig. S7. Tafel plots of as-synthesized $Ir/IrO_x/WO_3$ and $c\text{-}IrO_2$ in 0.5 M H_2SO_4.

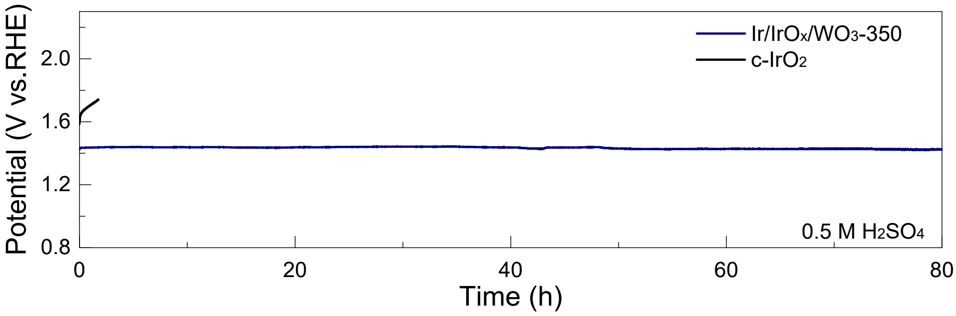

Fig. S8. Galvanostatic stability of the OER at the current density of 10 mA/cm^2 over as-synthesized $Ir/IrO_x/WO_3$ and $c\text{-}IrO_2$ in 0.5 M H_2SO_4.

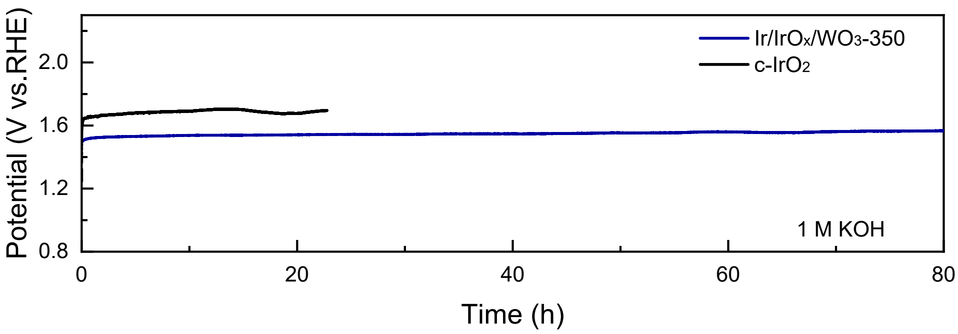

Fig. S9. Galvanostatic stability of the OER at the current density of 10 mA/cm^2 over d as-synthesized $Ir/IrO_x/WO_3$ and c-IrO_2 in 1.0 M KOH.

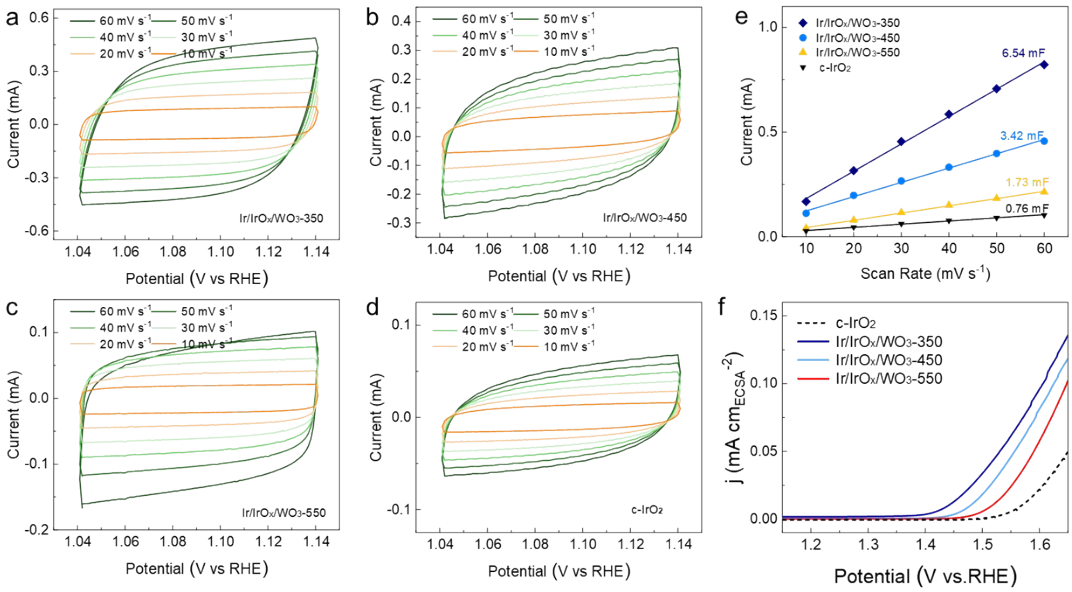

Fig. S10. CV curves of (a) $Ir/IrO_x/WO_3$ -350; (b) $Ir/IrO_x/WO_3$ -450; (c) $Ir/IrO_x/$ WO_3 -550; (d) c-IrO_2 collected at various scan rates (10, 20, 30, 40, 50 and 60 mV s^{-1}); (e) The double layer capacitance (C_{DL}) of as-synthesized $Ir/IrO_x/WO_3$ -350, $Ir/IrO_x/WO_3$-450, $Ir/IrO_x/$ WO_3 -550 and c-IrO_2; (f) Polarization curves (current normalized by ECSA) of as-synthesized $Ir/IrO_x/WO_3$ -350, $Ir/IrO_x/WO_3$-450, $Ir/IrO_x/$ WO_3 -550 and c-IrO_2.

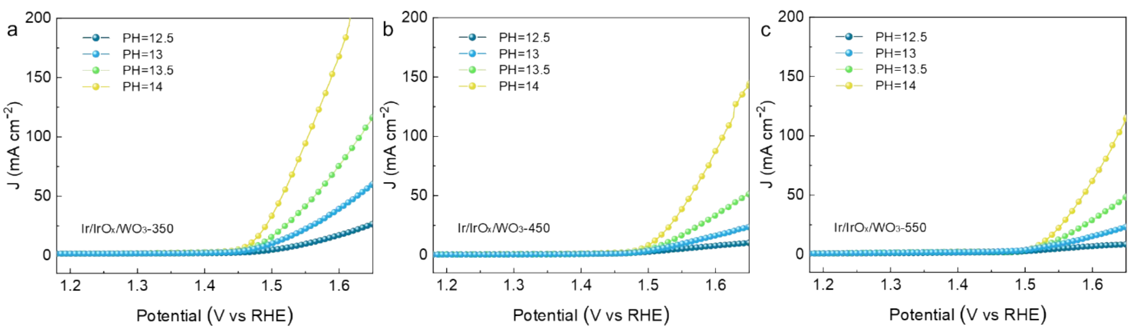

Fig. S11. pH dependence of the OER activities (a) $Ir/IrO_x/WO_3$-350; (b) $Ir/IrO_x/WO_3$ -450; (c) $Ir/IrO_x/$ WO_3 -550 in KOH.

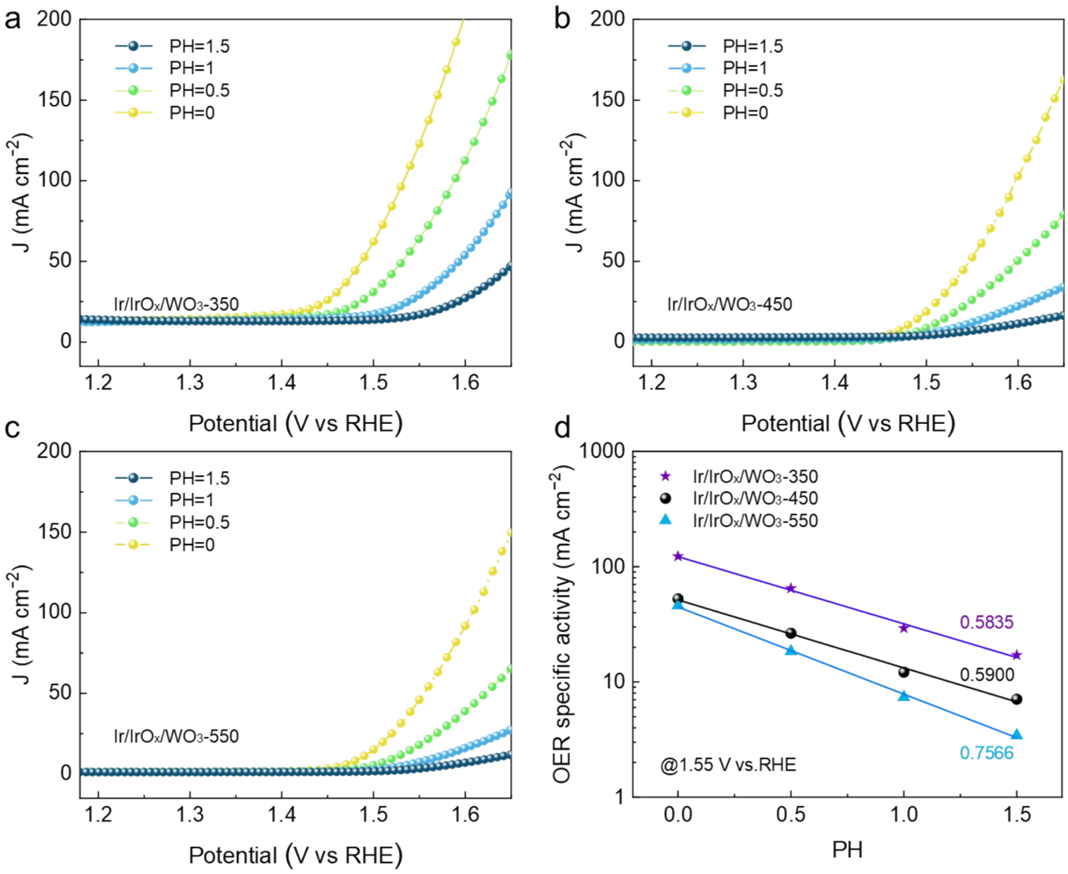

Fig. S12. pH dependence of the OER activities (a) $Ir/IrO_x/WO_3$-350; (b) $Ir/IrO_x/WO_3$ -450; (c) $Ir/IrO_x/$ WO_3 -550 in H_2SO_4; (d) Current densities of $Ir/IrOx/WO_3$-350, $Ir/IrOx/WO_3$-450 and $Ir/IrOx/WO_3$-550 at 1.55 V versus RHE as a function of the pH values of acidic electrolytes (H_2SO_4).

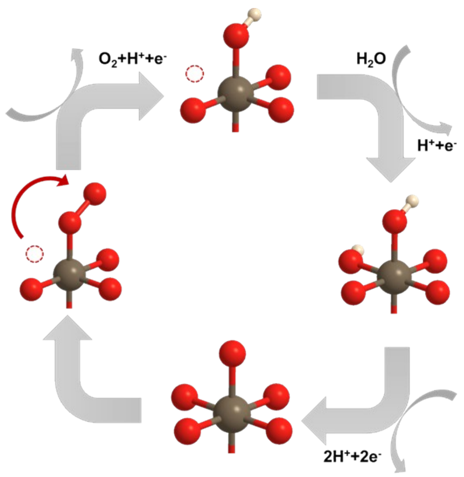

Fig. S13. OER mechanisms of LOM. The empty circle represents the oxygen vacancy. The gray, red and white balls represent Ir, O and H, respectively.

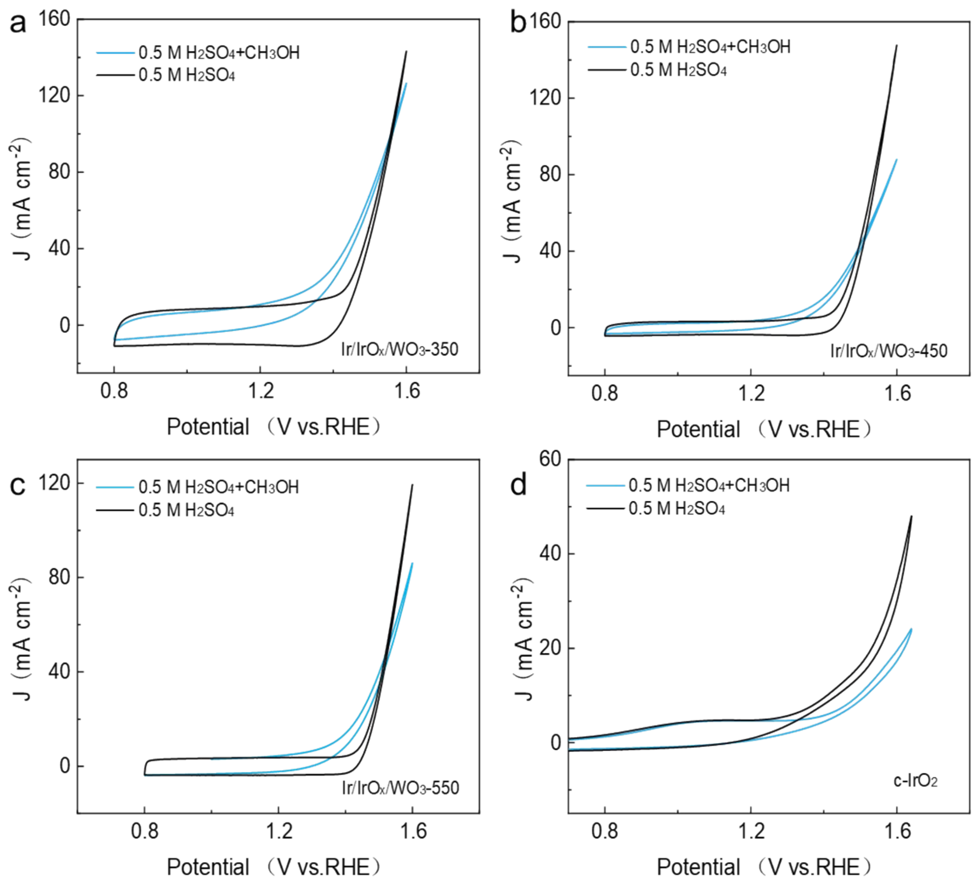

Fig. S14. CV curves of (a) Ir/IrO$_x$/WO$_3$-350; (b) Ir/IrO$_x$/WO$_3$ -450; (c) Ir/IrO$_x$/ WO$_3$ -550 and (d) c-IrO$_2$ at a scanning rate of 10 mV/s before and after adding methanol in 0.5 M H_2SO_4.

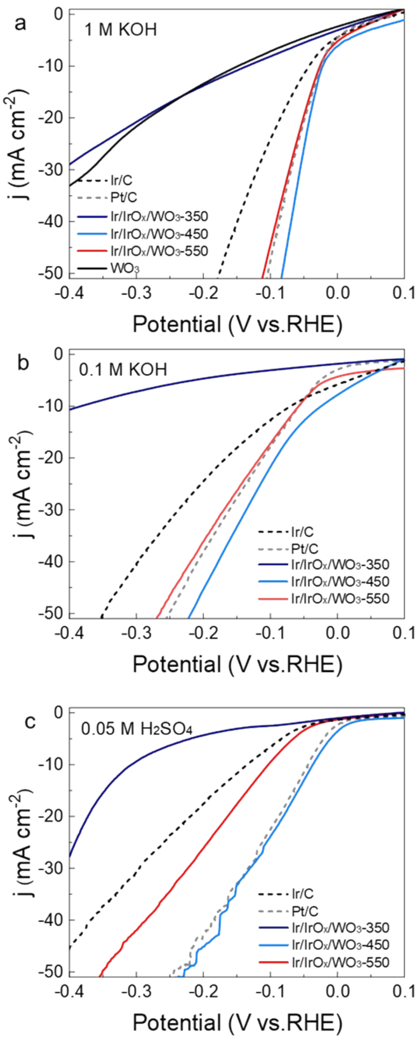

Fig. S15. Polarization curves of the as-synthesized Ir/IrO_x/WO_3-350, Ir/IrO_x/WO_3-450, Ir/IrO_x/WO_3-550, Ir/C and Pt/C in (a) 1.0 M KOH; (b) 0.1 M KOH; (c) 0.05 M H_2SO_4.

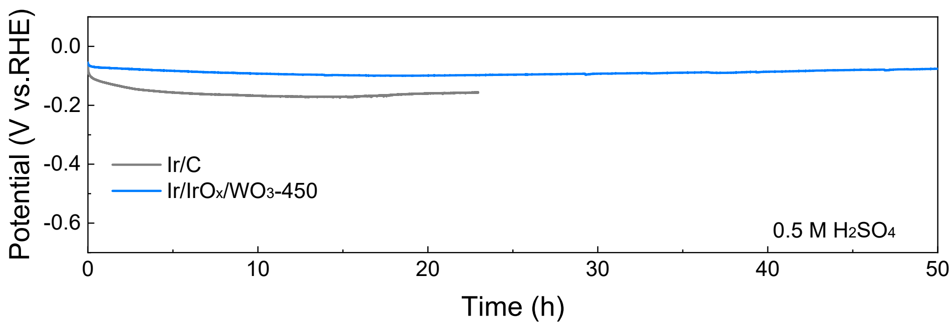

Fig. S16. Galvanostatic stability of the HER at the current density of 10 mA/cm^2 over as-synthesized Ir/IrO_x/WO_3 and Ir/C in 0.5 M H_2SO_4.

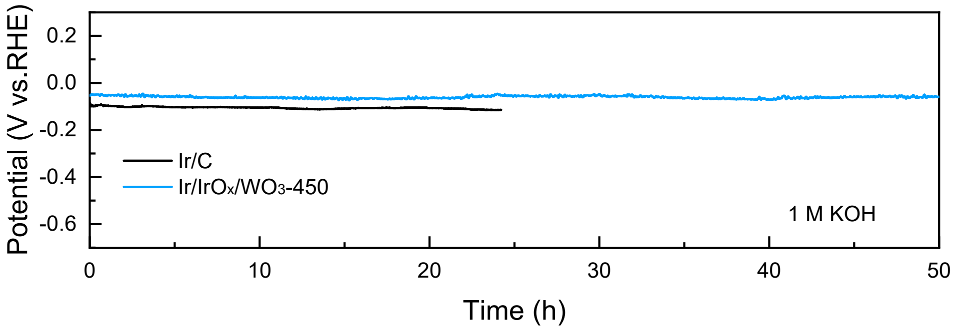

Fig. S17. Galvanostatic stability of the HER at the current density of 10 mA/cm^2 over as-synthesized Ir/IrO_x/WO_3 and Ir/C in 1.0 M KOH.

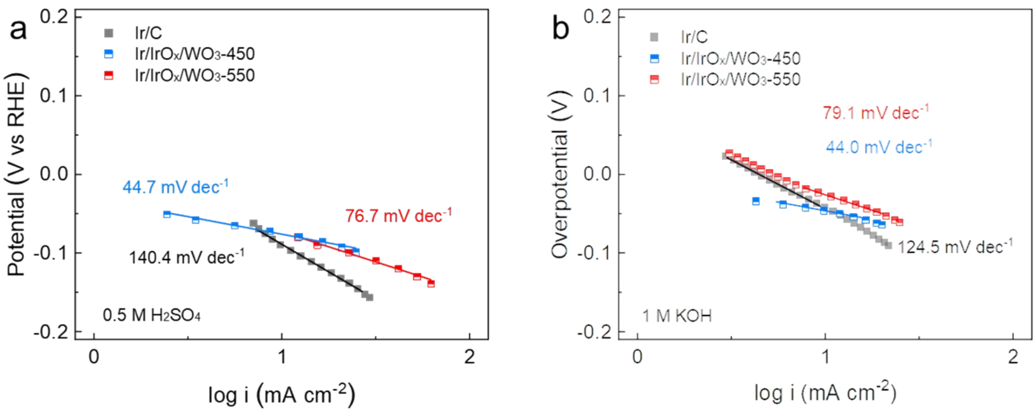

Fig. S18. Tafel slopes of Ir/IrO_x/WO_3 and Ir/C in (a) acid electrolyte and (b) alkaline electrolyte.

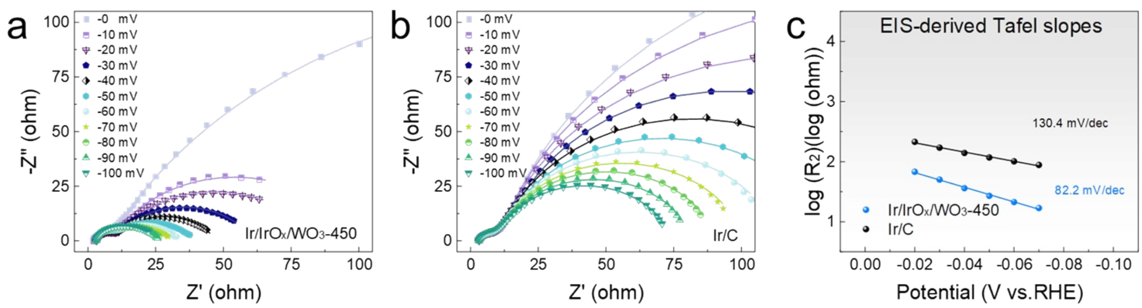

Fig. S19. (a) Ir/IrO_x/WO_3-450; and (b) Ir/C electrodes Nyquist graphs in 1.0 M KOH at various HER overpotentials. The dispersed symbols depict the experimental data, while the solid lines depict the simulated fitted outcomes. The similar circuit utilized in the simulation is shown in the top inset. (c) Tafel graphs in 1.0 M KOH produced from R_2 for Ir/IrO_x/WO_3-450 and Ir/C.

Table S5. The fitted parameters of the EIS data of the Ir/C electrode for HER.

Ir/C	R_s	CPE_2	n_2	R_2	C_{ads}
0	2.657	0.0012643	0.81215	341.5	0.000338
-0.01	3.146	0.001292	0.79992	406.7	0.000325
-0.02	3.1	0.0011776	0.81875	358.4	0.000339
-0.03	3.06	0.0012097	0.80505	351	0.000311
-0.04	3.075	0.001138	0.81613	310.1	0.000318
-0.05	3.066	0.0011242	0.81416	281.4	0.000307
-0.06	3.058	0.0011148	0.811183	247	0.000296
-0.07	3.071	0.0012129	0.78553	222.6	0.000262
-0.08	3.057	0.0012158	0.77946	183.9	0.000249
-0.09	3.074	0.0012024	0.7767	148	0.000239
-0.1	3.07	0.0012131	0.76782	122.2	0.000222

Table S6. The fitted parameters of the EIS data of the $Ir/IrO_x/WO_3$-450 electrode for HER.

$Ir/IrO_x/WO_3$-450	CPE_2	CPE_2	n_2	R_2	C_{ads}
0	3.009	0.0061876	0.76181	966.2	0.001779
-0.01	2.986	0.0059692	0.78386	710.9	0.001964
-0.02	2.936	0.0059603	0.78498	615.7	0.001965
-0.03	2.94	0.0059975	0.78155	457.9	0.001937
-0.04	2.943	0.0060444	0.76509	350.4	0.00175
-0.05	2.946	0.0060523	0.7565	229.9	0.001649
-0.06	2.97	0.0062793	0.72787	152.7	0.001407
-0.07	2.977	0.0063507	0.708	96.83	0.001221
-0.08	2.987	0.0071879	0.68781	59.28	0.00123
-0.09	2.979	0.0073367	0.65845	40.45	0.000973
-0.1	2.978	0.0079897	0.633114	28.1	0.000864

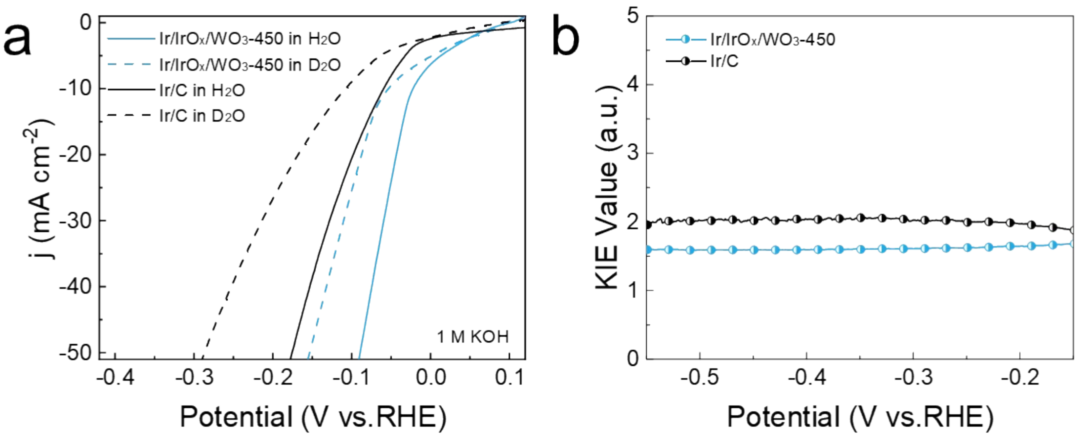

Fig. S20. (a) The polarization curves of $Ir/IrO_x/WO_3$-450 and Ir/C electrodes measured in H_2O or D_2O solution with 1.0 M KOH; (b) the ratio of the current density of electrocatalysts in H_2O to that in D_2O.

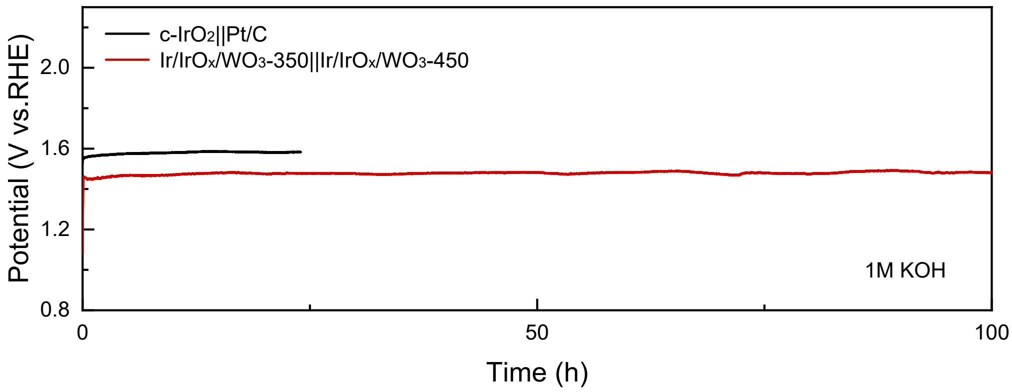

Fig. S21. Galvanostatic stability of the overall water splitting using $Ir/IrO_x/WO_3$-350 ll $Ir/IrO_x/WO_3$-450 and c-IrO_2 ll Pt/C catalyst operated at 10 mA/cm^2 in 1.0 M KOH.

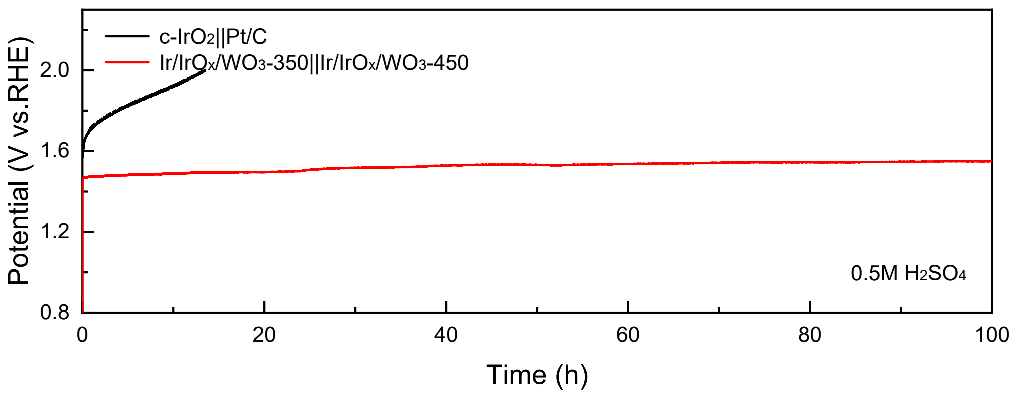

Fig. S22. Galvanostatic stability of the overall water splitting using $Ir/IrO_x/WO_3$-350ll $Ir/IrO_x/WO_3$-450 and c-IrO_2 ll Pt/C catalyst operated at 10 mA/cm^2 in 0.5 M H_2SO_4.

Table. S7. Summary of Ir-based and Ru-based catalysts for water splitting.

Catalyst	Electrolyte	Cell voltage (V)	Stability at 10 mA cm^{-2} (h)	Ref
$Ir/IrO_x/WO_3$	0.5M H_2SO_4; 1.0 M KOH	1.481; 1.481	100	This work
IrW ND	0.5M H_2SO_4; 1.0 M KOH	1.480; 1.548	8	16
IrW nanobranches	0.1 M $HClO_4$; 1.0 M KOH	1.580; 1.600	17	17
Ir VG	0.5M H_2SO_4; 1.0 M KOH	1.580; 1.570	-	18
Li-IrSe2	0.5M H_2SO_4; 1.0 M KOH	1.440; 1.480	1.47 V@24 h 1.52 V@24 h	19
Ir-NSs	0.5M H_2SO_4; 1.0 M KOH	1.586; 1.575	5 mA cm^{-2} @10 h	20
Ir-NR/C	0.5M H_2SO_4; 1.0 M KOH	1.550; 1.570	12	21
Ir-NSG	0.5M H_2SO_4; 1.0 M KOH	1.420; 1.450	24	22
P-IrOx@DG	0.5M H_2SO_4; 1.0 M KOH	1.480; 1.530	-	23
$Ru@MoO(S)_3$	0.5M H_2SO_4; 1.0 M KOH	1. 522; 1.526	24	24
RuCu NSs/C	0.5M H_2SO_4; 1.0 M KOH	1.490; 1.490	15	25

References

1 W.-H. Lai, L.-F. Zhang, W.-B. Hua, S. Indris, Z.-C. Yan, Z. Hu, B. Zhang, Y. Liu, L. Wang, M. Liu, R. Liu, Y.-X. Wang, J.-Z. Wang, Z. Hu, H.-K. Liu, S.-L. Chou and S.-X. Dou, General π-electron-assisted strategy for Ir, Pt, Ru, Pd, Fe, Ni single-atom electrocatalysts with bifunctional active sites for highly efficient water splitting, *Angew. Chem. Int. Ed.*, 2019, **58**, 11868-11873.

2 Q. Wang, X. Huang, Z. L. Zhao, M. Wang, B. Xiang, J. Li, Z. Feng, H. Xu and M. Gu, Ultrahigh-loading of Ir single atoms on NiO matrix to dramatically enhance oxygen evolution reaction, *J. Am. Chem. Soc.*, 2020, **142**, 7425-7433.

3 C. Cai, M. Wang, S. Han, Q. Wang, Q. Zhang, Y. Zhu, X. Yang, D. Wu, X. Zu, G. E. Sterbinsky, Z. Feng and M. Gu, Ultrahigh oxygen evolution reaction activity achieved using Ir single atoms on amorphous CoO_x nanosheets, *ACS Catal.*, 2021, **11**, 123-130.

4 Z. Li, D. Liu, X. Lu, M. Du, Z. Chen, J. Teng, R. Sha and L. Tian, Boosting oxygen evolution of layered double hydroxide through electronic coupling with ultralow noble metal doping, *Dalton Trans.*, 2022, **51**, 1527-1532.

5 J. Xu, Z. Lian, B. Wei, Y. Li, O. Bondarchuk, N. Zhang, Z. Yu, A. Araujo, I. Amorim, Z. Wang, B. Li and L. Liu, Acid-stable tellurium nanoparticle support for efficient and durable oxygen evolution in acidic and neutral media, *ACS Catal.*, 2020, **10**, 3571-3579.

6 G. Li, K. Li, L. Yang, J. Chang, R. Ma, Z. Wu, J. Ge, C. Liu and W. Xing, Boosted performance of Ir species by employing TiN as the support toward oxygen evolution reaction, *ACS Appl. Mater. Interfaces*, 2018, **10**, 38117-38124.

7 H.-S. Oh, H. N. Nong, T. Reier, M. Gliech and P. Strasser, Oxide-supported Ir nanodendrites with high activity and durability for the oxygen evolution reaction in acid PEM water electrolyzers, *Chem. Sci.*, 2015, **6**, 3321-3328.

8 J. Shan, C. Guo, Y. Zhu, S. Chen, L. Song, M. Jaroniec, Y. Zheng and S.-Z. Qiao, Charge-redistribution-enhanced nanocrystalline Ru@IrO_x electrocatalysts for oxygen evolution in acidic media, *Chem*, 2019, **5**, 445-459.

9 Z. Shi, Y. Wang, J. Li, X. Wang, Y. Wang, Y. Li, W. Xu, Z. Jiang, C. Liu, W. Xing and J. Ge, Confined Ir single sites with triggered lattice oxygen redox: Toward boosted and sustained water oxidation catalysis, *Joule*, 2021, **5**, 2164-2176.

10 K. Zhang, W. Mai, J. Li, H. Wang, G. Li and W. Hu, Highly scattered Ir oxides on TiN as an efficient oxygen evolution reaction electrocatalyst in acidic media, *J. Mater. Sci.,* 2020, **55**, 3507-3520.

11 Z. Lu, C. Wei, X. Liu, Y. Fang, X. Hao, Y. Zang, Z. Pei, J. Cai, Y. Wu, D. Niu, A. Mosallanezhad, D. Sun, J. Ye, S. Niu and G. Wang, Regulating the adsorption behavior of intermediates on Ir–W@Ir–WO_{3-x} boosts acidic water oxidation electrocatalysis, *Mater. Chem. Front.*, 2021, **5**, 6092-6100.

12 J. Chen, P. Cui, G. Zhao, K. Rui, M. Lao, Y. Chen, X. Zheng, Y. Jiang, H. Pan, S. X. Dou and W. Sun, Low-coordinate iridium oxide confined on graphitic carbon nitride for highly efficient oxygen evolution, *Angew. Chem., Int. Ed.*, 2019, **58**, 12540-12544.

13 G. Wu, X. Zheng, P. Cui, H. Jiang, X. Wang, Y. Qu, W. Chen, Y. Lin, H. Li, X. Han, Y. Hu, P. Liu, Q. Zhang, J. Ge, Y. Yao, R. Sun, Y. Wu, L. Gu, X. Hong and Y. Li, A general synthesis approach for amorphous noble metal nanosheets, *Nat. Commun.*, 2019, **10**, 4855.

14 H. Wang, Z.-n. Chen, D. Wu, M. Cao, F. Sun, H. Zhang, H. You, W. Zhuang and R. Cao, Significantly enhanced overall water splitting performance by partial oxidation of Ir through Au modification in core–shell alloy structure, *J. Am. Chem. Soc.*, 2021, **143**, 4639-4645.

15 F. Luo, H. Hu, X. Zhao, Z. Yang, Q. Zhang, J. Xu, T. Kaneko, Y. Yoshida, C. Zhu and W. Cai, Robust and stable acidic overall water splitting on Ir single atoms, *Nano Lett.*, 2020, **20**, 2120-2128.

16 F. Lv, J. Feng, K. Wang, Z. Dou, W. Zhang, J. Zhou, C. Yang, M. Luo, Y. Yang, Y. Li, P. Gao and S. Guo, Iridium–tungsten alloy nanodendrites as pH-universal water-splitting electrocatalysts, *ACS Cent. Sci.*, 2018, **4**, 1244-1252.

17 L. Fu, X. Hu, Y. Li, G. Cheng and W. Luo, IrW nanobranches as an advanced electrocatalyst for pH-universal overall water splitting, *Nanoscale*, 2019, **11**, 8898-8905.

18 S. B. Roy, K. Akbar, J. H. Jeon, S.-K. Jerng, L. Truong, K. Kim, Y. Yi and S.-H. Chun, Iridium on vertical graphene as an all-round catalyst for robust water splitting reactions, *J. Mater. Chem. A*, 2019, **7**, 20590-20596.

19 T. Zheng, C. Shang, Z. He, X. Wang, C. Cao, H. Li, R. Si, B. Pan, S. Zhou and J. Zeng, Intercalated iridium diselenide electrocatalysts for efficient pH-universal water splitting, *Angew. Chem. Int. Ed.,* 2019, **58**, 14764-14769.

20 Z. Cheng, B. Huang, Y. Pi, L. Li, Q. Shao and X. Huang, Partially hydroxylated ultrathin iridium

nanosheets as efficient electrocatalysts for water splitting, *Natl. Sci. Rev.*, 2020, **7**, 1340-1348.
21 F. Luo, L. Guo, Y. Xie, J. Xu, K. Qu and Z. Yang, Iridium nanorods as a robust and stable bifunctional electrocatalyst for pH-universal water splitting, *Appl. Catal. B*, 2020, **279**, 119394.
22 Q. Wang, C.-Q. Xu, W. Liu, S.-F. Hung, H. Bin Yang, J. Gao, W. Cai, H. M. Chen, J. Li and B. Liu, Coordination engineering of iridium nanocluster bifunctional electrocatalyst for highly efficient and pH-universal overall water splitting, *Nat. Commun.*, 2020, **11**, 4246.
23 L. Zhuang, F. Xu, K. Wang, J. Li, C. Liang, W. Zhou, Z. Xu, Z. Shao and Z. Zhu, Porous structure engineering of iridium oxide nanoclusters on atomic scale for efficient pH-universal overall water splitting, *Small*, 2021, **17**, 2100121.
24 D. Chen, R. Yu, D. Wu, H. Zhao, P. Wang, J. Zhu, P. Ji, Z. Pu, L. Chen, J. Yu and S. Mu, Anion-modulated molybdenum oxide enclosed ruthenium nano-capsules with almost the same water splitting capability in acidic and alkaline media, *Nano Energy*, 2022, **100**, 107445.
25 Q. Yao, B. Huang, N. Zhang, M. Sun, Q. Shao and X. Huang, Channel-rich RuCu nanosheets for pH-universal overall water splitting electrocatalysis, *Angew. Chem. Inter. Ed.*, 2019, **58**, 13983-13988.